Journal of Materials Chemistry A

ROYAL SOCIETY OF CHEMISTRY

PAPER

View Article Online
View Journal

Cite this: DOI: 10.1039/d0ta09520f

Ultrasensitive molecular sensing of few-layer niobium diselenide†

Qian Lv,‡[a] Xi Wu,‡[b] Junyang Tan,[b] Bilu Liu,[b] Lin Gan,[b] Jia Li,*[b] Zheng-Hong Huang,[ac] Feiyu Kang[bc] and Ruitao Lv*[ac]

Developing non-noble-metal-based materials with an excellent surface-enhanced Raman scattering (SERS) effect is indispensable for cost-effective, fast and nondestructive detection of trace amounts of molecules. Two-dimensional metallic transition metal dichalcogenides (TMDCs) are emerging in SERS fields by virtue of their ultra-flat atomic surface, high surface activity and abundant density of states (DOS) near the Fermi level. However, how to further decrease the limits of detection of TMDCs substrates is crucial but very challenging. In this contribution, large-area $NbSe_2$ flakes from monolayer to few-layer are controllably synthesized *via* an ambient pressure chemical vapor deposition route. The ultrasensitive SERS effect of $NbSe_2$ is demonstrated by optimizing the layer-dependent structure–effect correlation both experimentally and theoretically. As a proof of concept, Rhodamine 6G (R6G) molecules with an ultralow concentration of 5×10^{-16} M can be detected on 6L-$NbSe_2$, which is five orders of magnitude lower than that on 1L-$NbSe_2$. The ultrasensitive SERS effect of few-layer $NbSe_2$ is attributed to the strong adsorption energy and efficient charge transfer between R6G and $NbSe_2$ with specific layers induced by the highest DOS at the Fermi level. Our study provides new insight into the molecular sensing research of 2D TMDCs and paves the way for designing ultrasensitive SERS substrates.

Received 28th September 2020
Accepted 11th November 2020

DOI: 10.1039/d0ta09520f

rsc.li/materials-a

Introduction

Surface-enhanced Raman scattering (SERS) has attracted increasing attention in many fields, such as biomedicine,[1] environmental science,[2] chemistry,[3] and food security,[4] due to its fast, sensitive and nondestructive merits for detecting trace amounts of molecules or even a single molecule. Traditional SERS substrates are mainly based on roughened noble metals (*e.g.*, Au, Ag) by virtue of the electromagnetic mechanism (EM) excited by the localized surface plasmon resonance (LSPR).[5–7] Although excellent SERS performance could be achieved by using these substrates, the high cost, limited resources and low chemical stability of noble metals are still concerns to be addressed for their practical applications. The chemical mechanism (CM) is another SERS mechanism based on the charge-transfer process between the SERS substrates and probe molecules. Recently, two-dimensional (2D) layered materials, such as graphene,[8] MoS_2,[9] and WSe_2,[10] have emerged as very promising candidates for CM-based SERS substrates due to their ultra-flat atomic surface, good biocompatibility, and absence of dangling bonds compared with other non-2D nanomaterials,[11,12] which will facilitate the chemisorption of the probe molecules and further contribute to the acquisition of repeatable and stable Raman signals for practical applications. The adsorption energy and charge transfer between the substrates and the probe molecules play profound roles in the CM-driven SERS effects,[13,14] which are highly dependent on the band alignment between the substrates and the adsorbates. The electronic structures of 2D materials can be modulated by introducing dopants, vacancies, external fields (*e.g.*, strain and electricity), chemical functionalization or forming heterostructures.[15] In our previous works, the enhanced Raman scattering effects have been demonstrated by tailoring the electronic and chemical properties of graphene *via* doping heteroatoms into its sublattice, such as nitrogen,[8] silicon,[16] *etc.* Phase transition from the semiconducting 2H phase to the metallic 1T phase has also been applied to enhance the Raman scattering effect by improving the charge transfer between 1T-MoX_2 (X = S, Se) and probe molecules.[17] Moreover, introducing atomic vacancies in the lattice is also a feasible strategy to enhance the Raman scattering effect. Liu *et al.*[18] synthesized nonstoichiometric WSe_{2-x} (x = 0–0.08) by bombarding stoichiometric WSe_2 with

[a]State Key Laboratory of New Ceramics and Fine Processing, School of Materials Science and Engineering, Tsinghua University, Beijing 100084, China. E-mail: lvruitao@tsinghua.edu.cn

[b]Shenzhen Geim Graphene Center, Tsinghua Shenzhen International Graduate School, Tsinghua University, Shenzhen 518055, China. E-mail: li.jia@sz.tsinghua.edu.cn

[c]Key Laboratory of Advanced Materials (MOE), School of Materials Science and Engineering Tsinghua University, Beijing 100084, China

† Electronic supplementary information (ESI) available: Additional optical images, AFM morphologies, EDS spectra, atomic structures, Raman spectra, table of performance comparison, stacking models, and DFT curves. See DOI: 10.1039/d0ta09520f

‡ These authors contributed equally to this work.

an ion beam and the enhancement factor of WSe_{2-x} was 40 times higher than that of WSe_2. Although a series of defect/phase engineering strategies have been proposed to improve the SERS sensitivity of 2D layered materials, the limits of detection (LODs) in most previous reports are still no lower than $\sim10^{-9}$ M level, which is inferior to noble-metal-based substrates.[17,19–21] In order to further improve the probing sensitivity, it is imperative to develop non-noble-metal-based 2D layered materials with more efficient charge transfer as sensitive SERS substrates.

Recently, 2D metallic TMDCs have been explored as SERS substrates due to their abundant density of states (DOS) near the Fermi level and high surface activity, which contribute to the strong interface dipole–dipole coupling and efficient charge transfer with adsorbates to further enhance the Raman scattering cross-section.[22–24] Although previously studied 2D metallic TMDCs have achieved relatively low LODs (*e.g.*, 10^{-14} M), how to further decrease the LODs of TMDCs substrates for probing trace amounts of molecules to femtomolar levels or even higher sensitivity by electronic structure modulation is crucial but more challenging. Niobium diselenide ($NbSe_2$), a typical 2D metallic TMDCs, exhibits superconductivity, charge wave density, excellent photoconductivity, and especially a layer-dependent electronic structure, which provides a very promising candidate for the tunability and optimization of the SERS effect. In addition, $NbSe_2$ exhibits a higher Fermi level, which may facilitate the migration of electrons from the Fermi level to the highest occupied molecular orbital (HOMO) of molecules without extra energy, resulting in a higher electron transition probability and more enhanced SERS effect,[19] compared with semiconducting 2D TMDCs materials or monoelemental 2D materials with band gaps (*e.g.*, phosphorene).[25] Herein, we report the controllable synthesis of large-area $NbSe_2$ from monolayer to few-layer with the assistance of NaCl *via* an ambient pressure chemical vapor deposition (AP-CVD) route. The growth of thickness-tunable $NbSe_2$ could be achieved by precisely adjusting the experimental parameters (*e.g.*, Se supply, hydrogen content). Based on the as-grown samples, the ultrasensitive SERS performance of $NbSe_2$ by optimizing the correlation between the electronic structure and Raman scattering effect has been demonstrated both experimentally and theoretically for the first time. The Raman scattering of Rhodamine 6G (R6G) on six-layer (6L) $NbSe_2$ exhibits the highest sensitivity among the samples with different layers and the LOD can reach the subfemtomolar level ($\sim10^{-16}$ M), which is five orders of magnitude lower than that on monolayer $NbSe_2$, indicating the significance of interlayer coupling for the enhanced SERS effect. Density functional theory (DFT) calculations demonstrate that the ultrasensitive SERS effect of the as-grown $NbSe_2$ can be mainly attributed to the strong adsorption energy and efficient charge transfer between the probe molecules and as-grown $NbSe_2$. Most importantly, the layer-dependent structure–effect correlation of $NbSe_2$ is well established based on the DOS analysis at the Fermi level by DFT calculations. The DOS at the Fermi level of the outermost layer of 6L-$NbSe_2$, which is closely related to the interlayer coupling, is the highest, further indicating the most efficient charge transfer, which is in good agreement with our experimental results. Our results unveil the layer-dependent SERS effect of 2D metallic TMDCs from monolayer to few-layer, providing new insight into the rational design of efficient SERS substrates with optimal electronic structures to boost the molecular sensing capability.

Experimental section

Materials synthesis

Nb_2O_5 (99.9%, Alfa Aesar) and Se (99.9%, Alfa Aesar) powders were used as precursors for the $NbSe_2$ growth on SiO_2/Si wafers with a 270 ± 20 nm SiO_2 layer, and NaCl was used as an additive to promote the growth of $NbSe_2$. Before growth, the SiO_2/Si substrates were cleaned using piranha solution (a mixture of 98 wt% H_2SO_4 and 30 wt% H_2O_2 with a 3 : 1 volume ratio). Few-layer $NbSe_2$ was synthesized in a three-zone ambient pressure CVD system equipped with a 2-inch diameter quartz tube reactor. The mixture of Nb_2O_5/NaCl (240/70 wt/wt, ~3 mg) and Se powders (~2 g) were loaded to the center and left (L_{Se} = 5–7 cm, Fig. 1a) of the AP-CVD reactor, respectively. The SiO_2/Si substrate was placed on a quartz boat filled with a mixture of Nb_2O_5/NaCl, as shown in Fig. 1a. The quartz tube reactor was purged with ~1500 sccm argon (Ar) flow for ~10 min. Then, the furnace was heated up to 850 °C with 80 sccm Ar flow. Once reaching the set temperature, H_2 (6 sccm) was introduced for ~10 min for $NbSe_2$ growth. After the growth, the furnace was rapidly cooled down to room temperature by pulling the quartz tube out of the furnace. The synthesis of pristine graphene could be found in our previous report.[16] WSe_2 and $MoSe_2$ were synthesized based on the protocols reported in previous work.[26]

Materials characterization

An optical microscope (Olympus, BX 53) was used to characterize the morphology of samples. An atomic force microscope (AFM, Bruker DektakXT) was used to determine the thicknesses of samples. An X-ray photoelectron spectrometer (XPS, Thermo Fisher ESCALAB 250Xi) was used to analyze the chemical states. The binding energies were calibrated with C 1s at 284.8 eV. Transmission electron microscopy (TEM) was performed on an FET Tecnai TEM at an acceleration voltage of 300 kV.

SERS measurements

R6G/ethanol solutions with different concentrations (5×10^{-6}–5×10^{-16} M) were obtained by sequential diluting processes. The ethanol solutions of Methylene blue (MB) and Crystal violet (CV) were prepared with the same procedures as R6G. In a typical run, the $NbSe_2$ on SiO_2/Si substrate was immersed into the R6G solution for ~30 min, followed by rinsing with ethanol several times to remove the residual molecules and drying with nitrogen gas. The Raman spectra were recorded using a Horiba LabRAM HR Evolution system with a 500× objective and a laser spot size of ~1 μm. The excitation wavelength of the Raman laser for detecting R6G and CV is 532 nm, while for MB it is 633 nm.

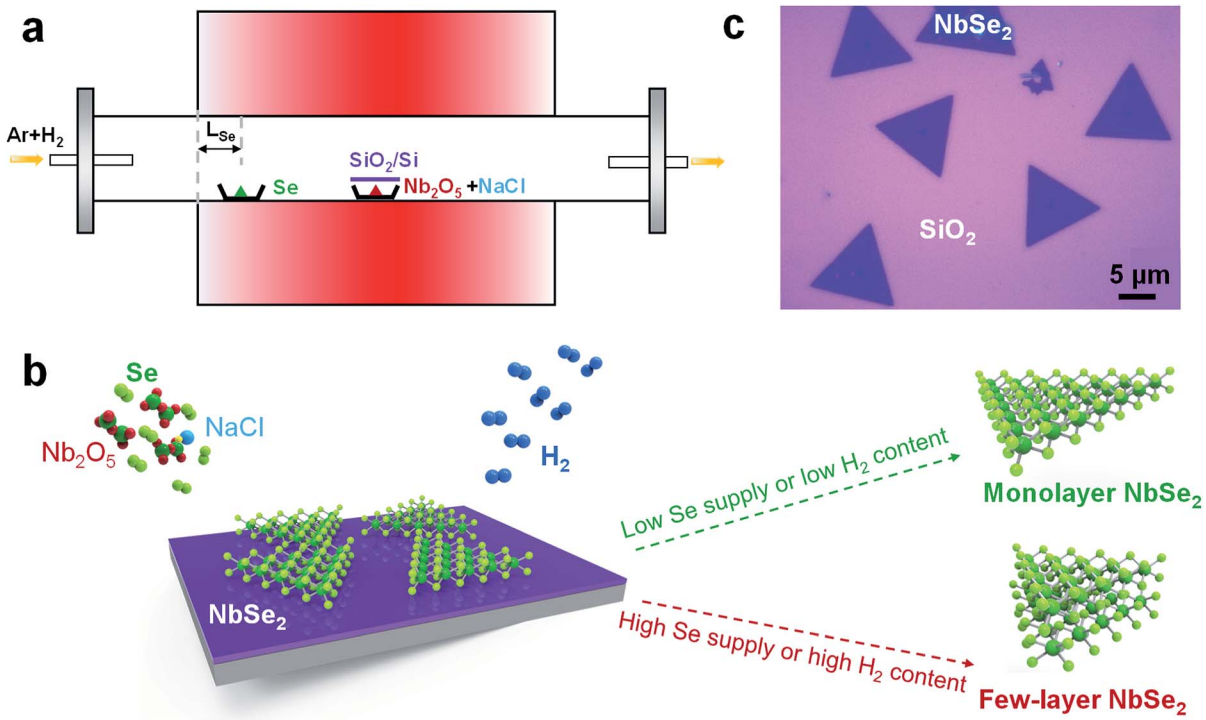

Fig. 1 Ambient pressure chemical vapor deposition (AP-CVD) growth of few-layer $NbSe_2$. (a) Schematic illustration of the AP-CVD setup for few-layer $NbSe_2$ growth. (b) Thickness-tunable growth of $NbSe_2$ by tuning the Se supply and the hydrogen content in Ar/H_2 carrier gas. (c) Typical optical image of the as-grown $NbSe_2$ on the SiO_2/Si substrate.

First principles calculations

Density functional theory (DFT) calculations were performed using the Vienna *ab initio* simulation package (VASP).[27] The projected augmented wave[28,29] and Perdew–Burke–Ernzerhof (PBE) functional[30,31] were used to describe the electron–ion interaction and exchange–correlation energy. To consider the van der Waals interaction between the layered $NbSe_2$, an empirical correction method, DFT-D3, was used.[32] To study the adsorption of R6G, a 7×7 supercell of 1L-$NbSe_2$ and 10×10 supercell of graphene were built with a vacuum layer of 20 Å. During the optimization, the energy cutoff was set at 400 eV, and the structure was allowed to fully relax until the energy converged to 10^{-5} eV and the residual force converged to 0.01 eV $Å^{-1}$. To study the DOS of $NbSe_2$ with different layers, the unit cell of $NbSe_2$ was built with a vacuum layer of 20 Å. To better distinguish the DOS of $NbSe_2$ with different layers, a $21 \times 21 \times 1$ Γ-centered k-mesh was used to sample the Brillouin zones, the energy cutoff was also increased to 520 eV, and energy convergence and residual force convergence were increased to 10^{-6} eV and 0.001 eV $Å^{-1}$, respectively.

Results and discussion

Atomically flat monolayer and few-layer $NbSe_2$ were synthesized on SiO_2/Si substrates with the assistance of NaCl by the AP-CVD method as illustrated in Fig. 1a and b. The quartz boat loaded with the mixture of Nb_2O_5 and NaCl powder was placed at the center of the AP-CVD reactor. Se vapor was transported from the upstream by Ar/H_2 carrier gas. The whole growth process was carried out at 850 °C for ~10 min. The addition of NaCl is essential for the growth of 2D TMDCs, which can react with transition metal oxide precursors to form intermediate compounds with lower melting points and further facilitate their growth.[33,34] In the meantime, Na^+ can act as an efficient catalyst to reduce the formation energy barrier of TMDCs during CVD growth.[35] 2D $NbSe_2$ with a triangular shape and uniform contrast can be obtained on the SiO_2/Si surface (Fig. 1c and S1, ESI†). In order to achieve the controllable synthesis of $NbSe_2$ with different layers, growth parameters during the AP-CVD process were systematically investigated. A scheme showing the influence of Se supply and hydrogen content in the carrier gas on the controllable growth of $NbSe_2$ is shown in Fig. 1b. It can be seen that the thicknesses and lateral sizes of the as-grown $NbSe_2$ are sensitive to the supply of Se vapor and hydrogen content in the carrier gas. The Se supply can be controlled by changing the locations of Se powder (L_{Se}) in the quartz tube (Fig. 1a). The higher value of L_{Se}, namely, higher temperature of the Se boat with more vapor supply, induces the growth of thicker and smaller $NbSe_2$ flakes (Fig. S2a–c, ESI†), which can be attributed to the fact that higher supply of Se vapor can accelerate the reaction with Nb_2O_5 and improve the nucleation density of $NbSe_2$. Similarly, the higher hydrogen content in the carrier gas can also promote the growth of thicker and smaller $NbSe_2$ flakes (Fig. S2d–f, ESI†). The reason lies in that hydrogen in the carrier gas could saturate the dangling bonds at the edge of the first grown flakes, and block the

epitaxial growth of flakes to improve the vertical growth,[36,37] leading to the growth of thicker and smaller flakes. The influences of Se supply and hydrogen content on the size of $NbSe_2$ are summarized in detail in Fig. S3 (ESI†). The AFM images show the as-grown $NbSe_2$ crystals with different thicknesses from ~1.1 to ~10.3 nm in Fig. S4 (ESI†), corresponding to $NbSe_2$ flakes from monolayer to more than ten layers.

Fig. 2a shows the typical Raman spectra of the as-grown $NbSe_2$ with different layers, all of which show two characteristic peaks at ~225 cm^{-1} and ~249 cm^{-1}, corresponding to the out-of-plane A_{1g} vibration mode and in-plane E_{2g} vibration mode of $NbSe_2$,[38] respectively. The strongest Raman intensity can be obtained on 6L-$NbSe_2$. Fig. 2d shows the Raman peak intensity mapping of the E_{2g} mode in monolayer $NbSe_2$ with uniform distributions, demonstrating its high crystal quality and uniform thickness.[39] The chemical valences of the as-grown $NbSe_2$ were examined by XPS (Fig. 2b and c). The deconvoluted Nb 3d core-level spectrum shows two pairs of doublet peaks at the low binding energy region (202–207 eV, pink and blue curves) assigned to Nb^{4+} $3d_{5/2}$ and Nb^{4+} $3d_{3/2}$, confirming the coexistence of hexagonal (2H) and rhombohedral (3R) phases in $NbSe_2$.[23,40] The other two peaks located at higher binding energy (207–210 eV, red curves in Fig. 2b) can be ascribed to Nb^{5+} $3d_{3/2}$ and Nb^{5+} $3d_{5/2}$,[41] which might be caused by the residual Nb_2O_5 particles (Fig. S5, ESI†).[23,42] The energy-dispersive X-ray spectrometry (EDS) elemental mapping and spectra of $NbSe_2$ crystals further demonstrate that the Nb^{5+} peaks in the Nb 3d XPS spectrum are not derived from the oxidation of the as-grown $NbSe_2$ in terms of the nearly absent oxygen peak in Fig. S6 (ESI†). The Se 3d core-level spectrum can also be deconvoluted into two pairs of doublet peaks assigned to Se^{2-} $3d_{5/2}$ and Se^{2-} $3d_{3/2}$ (Fig. 2c), which is consistent with the results of Nb 3d peaks of 2H-$NbSe_2$ (pink curves) and 3R-$NbSe_2$ (blue curves) of the as-grown $NbSe_2$.[23,43]

TEM characterization was carried out to reveal the microstructure and crystallinity of the as-grown $NbSe_2$ flakes. High-resolution TEM (HRTEM) images reveal the existence of a hexagonal atomic lattice with two stacking orders (Fig. 2e and

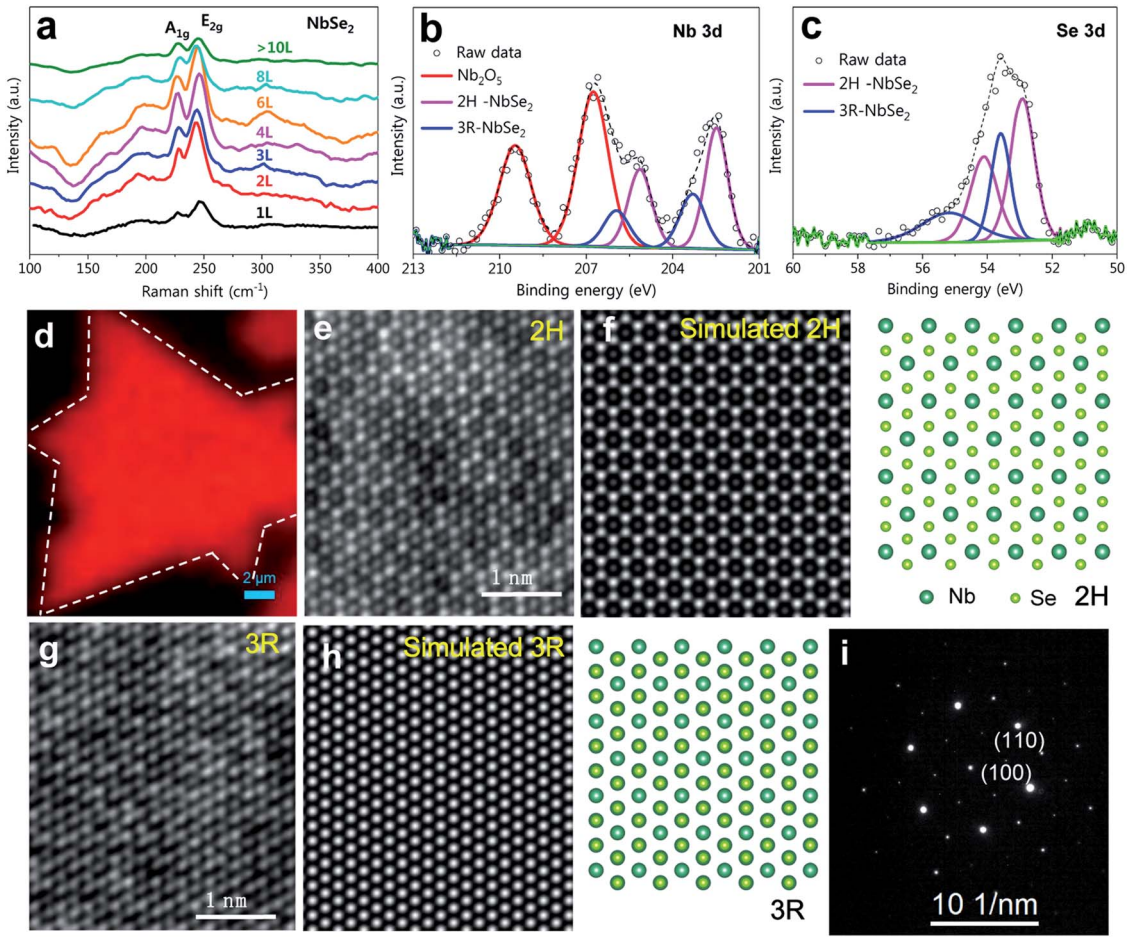

Fig. 2 Structural and compositional characterizations of the as-grown $NbSe_2$. (a) Raman spectra of the as-grown $NbSe_2$ with different layers. (b and c) X-ray photoelectron spectroscopy (XPS) fine scan spectra of the Nb 3d and Se 3d of the as-grown $NbSe_2$. The appearance of Nb_2O_5 peaks might be ascribed to the residual Nb_2O_5 precursor. (d) Raman mapping of the E_{2g} mode of the as-grown $NbSe_2$. (e and f) Experimental (e) and simulated (f) high-resolution transmission electron microscope (HRTEM) images of 2H-$NbSe_2$. (g and h) Experimental (g) and simulated (h) HRTEM images of 3R-$NbSe_2$. The image simulation was conducted at a sample thickness of 8 nm and a defocus value of −30 nm. (i) Selected-area electron diffraction (SAED) pattern of the as-grown $NbSe_2$.

g), which can be assigned to the 2H and 3R stacking modes of $NbSe_2$,[23,40,44] respectively. The HRTEM image of the 2H-$NbSe_2$ exhibits alternating dark and bright spots (Fig. 2e), which can be further confirmed by the simulated result (Fig. 2f), which presents an A′B stacking mode with the inverse orientation (A and B denote the orientation; "′" denotes the stacking sequence) (Fig. S7a and b, ESI†), while 3R-$NbSe_2$ follows a staggered AA stacking mode with an identical orientation but an in-plane shift (Fig. S7c and d, ESI†). The simulated image of 3R-$NbSe_2$ (Fig. 2h) matches well with the experimental HRTEM image (Fig. 2g), in which each spot shows nearly the same intensity. Moreover, we observe that the 2H arrangement dominates the as-grown $NbSe_2$ stacking mode, which is the common polymorph in bulk $NbSe_2$. Also, the corresponding selected area electron diffraction (SAED) pattern shows the typical orientation-matched hexagonal lattice feature of few-layer $NbSe_2$ (Fig. 2i). Taken together, the above results demonstrate the coexistence of 2H and 3R phases in the as-grown $NbSe_2$, but the 2H phase is the dominating one.

To evaluate the SERS effect of the as-grown $NbSe_2$, as a proof of concept, R6G is used as the probe molecule, as illustrated in Fig. 3a. The as-grown $NbSe_2$ on the SiO_2/Si substrate was immersed in R6G solution with a concentration of 5×10^{-6} M for ~30 min, then the sample was rinsed with ethanol several times and then dried with nitrogen gas. To maximize the Raman signals by complementary resonance effects, the wavelengths of probe molecules and charge transfer resonances should be well matched with the excitation wavelength of the laser.[45] For R6G and CV, their Raman signals can be mostly excited by a 532 nm laser, while for MB, the Raman signals can be mostly excited by a 633 nm laser, which are decided by the energy level differences between the HOMO and the lowest unoccupied molecular orbital (LUMO) of the probe molecules.[46–48] Thus, the excitation wavelength of the laser for R6G and CV was set at 532 nm, while for MB, it was set at 633 nm. The Raman spectra of R6G were collected from bare SiO_2/Si and $NbSe_2$, respectively, as shown in Fig. S8 (ESI†). It can be seen that the Raman signals of R6G can be hardly detected on bare SiO_2/Si due to the strong fluorescence effect. In sharp contrast, the as-grown $NbSe_2$ can efficiently quench the fluorescence effect and the Raman vibrational modes of R6G on $NbSe_2$ can be clearly distinguished marked by "◆", demonstrating the significantly enhanced Raman scattering effect of $NbSe_2$ as a SERS substrate. Considering the unique electronic structures of 2D TMDCs depending on layer numbers, the correlation between the electronic structure of the as-grown $NbSe_2$ with different layers and Raman scattering effect was investigated and the results are shown in Fig. 3b. The Raman intensity of R6G shows no distinct differences on $NbSe_2$ from monolayer to three layers. Subsequently, the Raman intensity of R6G gradually becomes stronger with further increasing the $NbSe_2$ layer numbers (n) until it reaches the maximum when $n = 6$. Upon further increasing the n value, the Raman intensity of R6G will decrease. This structure–effect correlation of $NbSe_2$ substrate is very different from those of MoS_2 (ref. 49) and ReS_2,[50] which exhibit gradually decreased Raman intensities of probe molecules with increasing the number of layers. It is well known that the enhanced Raman scattering effect is closely related to the band alignment between the 2D materials and the probe molecules. These different structure–effect correlations of various TMDCs substrates may be related to their carrier transportation behaviours depending on semiconducting or

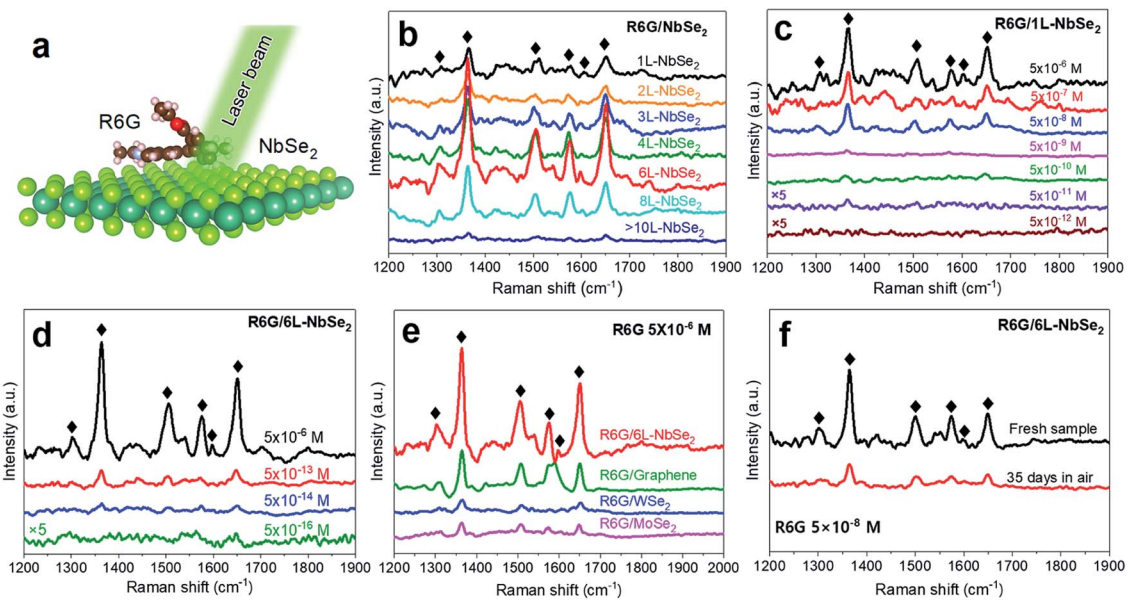

Fig. 3 Surface-enhanced Raman scattering (SERS) effect of the as-grown $NbSe_2$. (a) Schematic illustration of the as-grown $NbSe_2$ serving as a SERS substrate for probing R6G molecules excited by a 532 nm laser. (b) Layer-dependent Raman spectra of R6G on $NbSe_2$ with a concentration of 5×10^{-6} M. (c and d) Raman spectra of R6G with different concentrations ranging from 5×10^{-6} to 5×10^{-16} M on monolayer $NbSe_2$ (1L-$NbSe_2$) and 6-layer $NbSe_2$ (6L-$NbSe_2$). (e) The SERS effect comparison among different 2D materials with the R6G concentration of 5×10^{-6} M. (f) Raman spectra of R6G (5×10^{-8} M) on 6L-$NbSe_2$ after exposure in air for more than one month (35 days).

metallic phases, in which semiconducting and metallic phases exhibit different electronic structures induced by the layer-dependent interlayer coupling. Besides, the molecular configuration with 2D substrates and chemisorption capability of molecules on 2D materials may also be related to the layer-dependent SERS effects.[24,49,51] The Raman intensities of R6G on 6L-$NbSe_2$ at 1361 cm^{-1} and 1646 cm^{-1} are ~5 and ~3 times stronger than those on 1L-$NbSe_2$ (Fig. S9a, ESI†), respectively. The LOD, *i.e.*, the lowest detectable concentration of molecules, is a key indicator to evaluate the sensitivity of SERS substrates. Hence, a series of diluted R6G solutions with concentrations ranging from 5×10^{-6} to 5×10^{-16} M were prepared and tested in Fig. 3c. The Raman signals of R6G on 1L-$NbSe_2$ are still detectable until the concentration falls to 5×10^{-11} M, which is comparable to the lowest detectable concentration of nitrogen-doped graphene (NG).[46] More importantly, the LOD of R6G on 6L-$NbSe_2$ can even be lowered down to 5×10^{-16} M at the subfemtomolar level (Fig. 3d), which is five orders of magnitude lower than that on 1L-$NbSe_2$, indicating the ultrasensitive SERS performance of few-layer $NbSe_2$ for probing molecules. The relationships between Raman intensities and R6G concentrations on 1L- and 6L-$NbSe_2$ at 1361 cm^{-1} and 1646 cm^{-1} are summarized in Fig. S9b and c (ESI†), respectively. The uniform Raman peak intensity mapping of R6G on $NbSe_2$ indicates that the probe molecules are homogeneously adsorbed on the surface of $NbSe_2$. Also, a uniform Raman scattering enhancement of R6G molecules on the as-grown $NbSe_2$ is achieved (Fig. S10, ESI†). Moreover, AFM was used to characterize the morphological changes of $NbSe_2$ before and after R6G adsorption (Fig. S11a–c, ESI†). It can be seen that after soaking in R6G/ethanol solution with high concentration (*e.g.*, 5×10^{-5} M), there are many clusters on the $NbSe_2$ surface even after rinsing with ethanol serval times. However, when the concentration of R6G is lowered down to 5×10^{-6} M, the R6G clusters significantly decrease. Upon further decreasing the R6G concentration down to 5×10^{-11} M, the clusters almost disappear, showing almost no difference from bare $NbSe_2$ (see Fig. S4, ESI†). Our previous work and studies from other groups have already demonstrated that the adsorbed dye molecules can be regarded as a submonolayer when the concentration of molecules was lower than 10^{-6} to 10^{-7} M both experimentally and theoretically.[13,46]

A series of control experiments were carried out to compare the SERS effects of the as-grown $NbSe_2$ with those of other 2D materials grown *via* the AP-CVD route, such as graphene, WSe_2 and $MoSe_2$. The Raman spectra of these 2D materials are shown in Fig. S12 (ESI†). Fig. 3e shows the Raman spectra of R6G on different 2D materials. R6G molecules on 6L-$NbSe_2$ show the strongest Raman signals, followed by those on graphene, while the R6G molecules on WSe_2 and $MoSe_2$ show the weakest Raman signals, mainly ascribed to their semiconducting nature and weakly polar Se–Mo(W)–Se bonds leading to the limited charge transfer and weak dipole–dipole interactions with probe molecules.[45] Fig. 4a summarizes the Raman intensities of R6G at 1361 cm^{-1} and 1646 cm^{-1} on various 2D materials. The enhanced Raman intensities of R6G at 1361 cm^{-1} and 1646 cm^{-1} on 6L-$NbSe_2$ are ~9 and ~10 times higher than those on semiconducting WSe_2, respectively. Fig. 4b summarizes the SERS performances of probe molecules on the state-of-the-art 2D substrates reported in recent years, including pure graphene (PG),[14] 1T-MoS_2,[19] few-layer MoS_2,[20] 2H-NbS_2,[23] 1T′-ReS_2,[50] 1T′-WTe_2,[24] and NG.[46] We can see that 6L-$NbSe_2$ in this work exhibits a record low LOD compared to other state-of-the-art 2D materials. This superior SERS performance of 6L-$NbSe_2$ might be ascribed to the strong interface coupling interactions between $NbSe_2$ layers originating from the tightly bonded metallic bonds,[52] which can tailor the electronic structures (*e.g.*, DOS) and further strengthen the adsorption energy and electron transition probability between the 6L-$NbSe_2$ substrate and molecules. A detailed SERS effect comparison among various substrates is presented in Table S1 (ESI†).

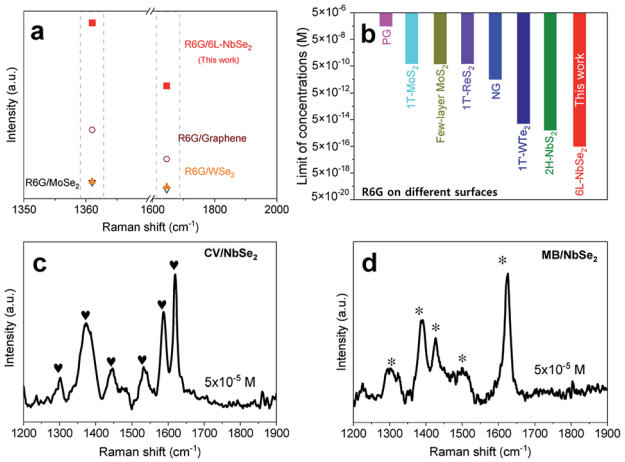

Fig. 4 (a) Comparison of Raman peak intensities of R6G at 1361 and 1646 cm^{-1} on different two-dimensional (2D) materials. (b) Summary of limits of detection (LODs) for recently reported 2D materials: PG, 1T-MoS_2, few-layer MoS_2, 1T′-ReS_2, NG, 1T′-WTe_2, and 2H-NbS_2. PG and NG denote as pristine graphene and N-doped graphene, respectively. (c and d) Raman spectra of crystal violet (CV) (c) and methylene blue (MB) (d) on the as-grown $NbSe_2$ for verifying the universal capability. Symbols "♥" and "*" represent the typical peaks of CV and MB, respectively.

The long-term stability and universality of the as-grown $NbSe_2$ as a SERS substrate were also evaluated. In general, 2D metallic TMDC materials tend to be oxidized and adsorb impurities under ambient conditions due to the existence of some defects (*e.g.*, vacancies and grain boundaries).[40,53] In order to minimize the existence of Se vacancies with relatively high energy, excess Se vapor was supplied during $NbSe_2$ growth, which can improve its stability in the atmosphere by decreasing the whole energy of $NbSe_2$. Even after being exposed in air for more than one month (35 days), there are still detectable Raman signals of R6G on the 6L-$NbSe_2$ surface (Fig. 3f), demonstrating the excellent stability of 6L-$NbSe_2$ in air and the strong adsorption of probe molecules on its surface. In addition, theoretical calculations have revealed that the ambient impurities of C, N and O can substitute into the $NbSe_2$ lattice to stabilize Se vacancies,[54] which might also be beneficial to improve the stability of $NbSe_2$ in air. Meanwhile, the stability of 2D TMDCs materials also shows a certain improvement with the increasing of layers compared with monolayer

ones. Besides R6G molecules, the as-grown $NbSe_2$ can detect other molecules, such as CV, MB, *etc.*, as shown in Fig. 4c and d, respectively, and the typical Raman peaks of each molecule are marked by "♥" and "*", respectively, suggesting that the SERS effect of the as-grown $NbSe_2$ can be applied for probing other organic molecules.

Considering that the atomically flat surfaces were hardly able to support EM enhancement and the plasmon resonance peak of $NbSe_2$ occurs in the infrared region rather than visible region,[51,55,56] the EM-driven SERS effect in the R6G/$NbSe_2$ system excited by a 532 nm laser can be excluded. DFT calculations were used to scrutinize the interaction and charge transfer process between R6G and the as-grown $NbSe_2$ (graphene as a reference) mainly based on the CM-driven SERS effect. Three adsorption configurations of R6G are considered on $NbSe_2$ and graphene, respectively, and their optimized adsorption structures are shown in Fig. 5a and b. The adsorption energies of R6G on $NbSe_2$ and graphene in the most stable configurations are −2.65 eV and −1.62 eV, respectively, indicating that the R6G molecules exhibit much stronger interaction with $NbSe_2$ than with graphene. The differences in the interaction of R6G/$NbSe_2$ and R6G/graphene can be reflected by the charge density difference of the R6G/$NbSe_2$ and R6G/graphene, as shown in Fig. 5c and d. For the R6G/$NbSe_2$, a charge redistribution appeared at the interface, and a charge of about 0.74*e* was determined to be transferred from the R6G molecule to the $NbSe_2$ layer. However, the charge transferred from R6G to graphene is only 0.13*e*. Thus, the stronger adsorption energy and more efficient charge transfer between R6G and $NbSe_2$ endow $NbSe_2$ with much more sensitive SERS performance than other 2D materials.

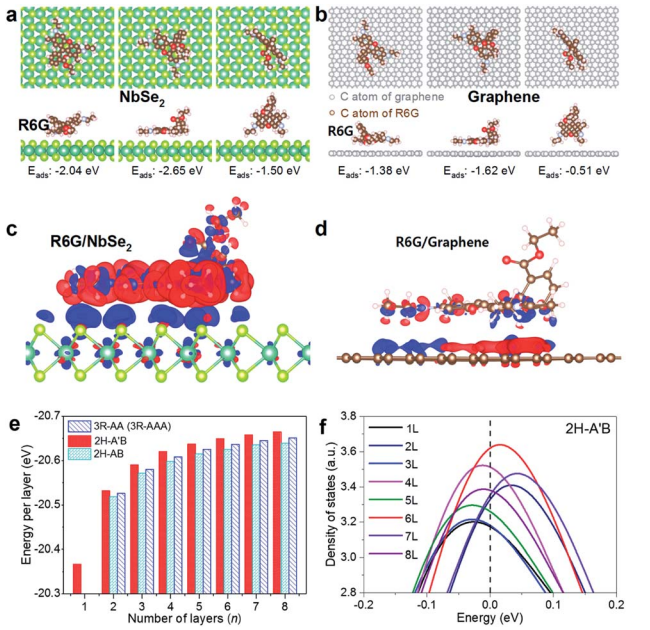

Fig. 5 Density functional theory (DFT) calculation results of R6G adsorption on $NbSe_2$ and graphene. (a and b) Top and side views of R6G molecules adsorbed on the as-grown $NbSe_2$ (a) and graphene (b). (c and d) Charge density difference of R6G adsorption on the as-grown $NbSe_2$ (c) and graphene (d). (e) Formation energy of the as-grown $NbSe_2$ with different stacking modes. (f) Density of states (DOS) of the outermost layer of 2H-$NbSe_2$ with different layers in the A′B stacking mode. The Fermi level was set to zero. For charge density difference, blue (red) corresponds to charge accumulation (depletion) plotted with an isovalue of ±0.002 e $Å^{-3}$.

In order to elucidate the correlation between the structures and SERS effects of the as-grown $NbSe_2$, we investigated the electronic structures of $NbSe_2$ from monolayer to eight layers by DFT calculations. We first determine the most stable stacking mode of $NbSe_2$. Five typical stacking modes of $NbSe_2$,[57] 2H phase with A′B and AB stacking modes (marked as 2H-A′B and 2H-AB), and 3R phase with AA′, AA and AAA stacking modes (marked as 3R-AA′, 3R-AA and 3R-AAA), are considered (Fig. S13, ESI†). From monolayer to eight layers of $NbSe_2$, the 2H-A′B stacking mode of $NbSe_2$ possesses the lowest energy per layer, while the 2H-AB phase of $NbSe_2$ has the highest energy per layer (Fig. 5e). Note that 3R-AA′ stacking modes are unstable and would transform into the relatively stable 3R-AA (or 3R-AAA) stacking modes during the structure optimization, because 3R-AA and 3R-AAA stacking modes exhibit nearly the same energy per layer. Thus, the 2H-A′B phase is the most stable stacking mode of $NbSe_2$, followed by the 3R-AA phase, which can explain the coexistence of 2H-A′B and 3R-AA phases in the as-grown $NbSe_2$. The DOS of the outermost $NbSe_2$ layer with 2H-A′B and 3R-AA stacking modes with different layers are shown in Fig. S14–S17 (ESI†), while the detailed DOSs at the Fermi level of 2H-A′B $NbSe_2$ from monolayer to eight layers are illustrated in Fig. 5f. For 2H-A′B phase, the outermost layer of 6L-$NbSe_2$ possesses the highest DOS value at the Fermi level, which is beneficial for the improvement of the electron transition probability rate with probe molecules, giving rise to the most efficient charge transfer process. Our DFT calculations match well with the experimental results. The relationship between electronic structure and Raman scattering effect of $NbSe_2$ with different layers is well illustrated by experimental results and theoretical calculations, which provides guidance to understand the structure–effect correlations of metallic TMDCs as SERS substrates and may be insightful for the further material optimization. Although the ultrasensitive SERS effect of the as-grown $NbSe_2$ has been well elucidated experimentally and theoretically, the stability of $NbSe_2$ under ambient conditions is still not comparable to that of semiconducting ones. Therefore, we will continue to work on the improvement of $NbSe_2$ stability in the future. And, further improving the probe sensitivity to achieve the single molecular sensing level (*e.g.*, 10^{-18} M) will be more challenging but significant.[58] With the emergence of various portable, especially wearable smart electronic products, the demand for flexible sensing devices is gradually increasing.[59] Thus, transferring $NbSe_2$ single-crystalline film onto flexible substrates to construct flexible devices will be indispensable for their practical applications in the sensing fields in the future.

Conclusions

In summary, we synthesized large-area and high-quality $NbSe_2$ from monolayer to few-layer by AP-CVD route with the

assistance of NaCl. The higher Se supply and hydrogen content guarantee the growth of few-layer $NbSe_2$. Meanwhile, the higher Se supply can minimize the presence of Se vacancies, leading to a better stability of the as-grown $NbSe_2$ in air. Raman scattering of R6G can be remarkably excited on the 6L-$NbSe_2$ surface with an ultralow LOD of 5×10^{-16} M at the subfemtomolar level, which is five orders of magnitude lower than that on 1L-$NbSe_2$ and superior to that of many state-of-the-art metallic 2D materials and comparable or even superior to that of noble-metal-based materials. The ultrasensitive SERS effect can be attributed to the strong adsorption energy and efficient charge transfer between the R6G molecules and $NbSe_2$ substrate. More importantly, DFT calculations elucidate the structure–effect correlation of $NbSe_2$ with different layers as SERS substrates, in which 6L-$NbSe_2$ exhibits the highest DOS at the Fermi level and contributes to the high electron transition probability rate with the probe molecules compared to $NbSe_2$ with other layer numbers. Our results suggest that few-layer $NbSe_2$ can serve as a very promising SERS candidate and might be applied in other sensing fields, such as biomolecule detection, food safety, homeland security, *etc.*

Conflicts of interest

There are no conflicts to declare.

Acknowledgements

This work was supported by the National Natural Science Foundation of China (Grant No. 51722207, 51972191, 11874036 and 51920105002), the Guangdong Province Key Area R&D Program (2019B010940001), the Local Innovative and Research Teams Project of Guangdong Pearl River Talents Program (Grant No. 2017BT01N111), Basic Research Project of Shenzhen, China (Grant No. JCYJ20170412171430026), and the Bureau of Industry and Information Technology of Shenzhen for the "2017 Graphene Manufacturing Innovation Center Project" (No. 201901171523). We thank Prof. Hui-Ming Cheng and Dr Simin Feng for the fruitful discussion and important advice regarding this work.

Notes and references

1 X. Qiao, B. Su, C. Liu, Q. Song, D. Luo, G. Mo and T. Wang, *Adv. Mater.*, 2017, **30**, 1702275.
2 R. A. Halvorson and P. J. Vikesland, *Environ. Sci. Technol.*, 2010, **44**, 7749.
3 J. Lin, Y. Shang, X. Li, J. Yu, X. Wang and L. Guo, *Adv. Mater.*, 2017, **29**, 1604797.
4 A. P. Craig, A. S. Franca and J. Irudayaraj, *Annu. Rev. Food Sci. Technol.*, 2013, **4**, 369.
5 G. Eom, H. Kim, A. Hwang, H.-Y. Son, Y. Choi, J. Moon, D. Kim, M. Lee, E.-K. Lim, J. Jeong, Y.-M. Huh, M.-K. Seo, T. Kang and B. Kim, *Adv. Funct. Mater.*, 2017, **27**, 1701832.
6 A. Chen, A. E. DePrince, A. Demortiere, A. Joshi-Imre, E. V. Shevchenko, S. K. Gray, U. Welp and V. K. Vlasko-Vlasov, *Small*, 2011, **7**, 2365.
7 C. Matricardi, C. Hanske, J. L. Garcia-Pomar, J. Langer, A. Mihi and L. M. Liz-Marzan, *ACS Nano*, 2018, **12**, 8531.
8 R. T. Lv, Q. Li, A. R. Botello-Mendez, T. Hayashi, B. Wang, A. Berkdemir, Q. Z. Hao, A. L. Elias, R. Cruz-Silva, H. R. Gutierrez, Y. A. Kim, H. Muramatsu, J. Zhu, M. Endo, H. Terrones, J.-C. Charlier, M. H. Pan and M. Terrones, *Sci. Rep.*, 2012, **2**, 586.
9 C. Muehlethaler, C. R. Considine, V. Menon, W.-C. Lin, Y.-H. Lee and J. R. Lombardi, *ACS Photonics*, 2016, **3**, 1164.
10 Y. Tan, L. Ma, Z. Gao, M. Chen and F. Chen, *Nano Lett.*, 2017, **17**, 2621.
11 S. Yang, Y. Liu, W. Chen, W. Jin, J. Zhou, H. Zhang and G. S. Zakharova, *Sensor. Actuator. B Chem.*, 2016, **226**, 478.
12 J. Liu, X. Jiang, R. Zhang, Y. Zhang, L. Wu, W. Lu, J. Li, Y. Li and H. Zhang, *Adv. Funct. Mater.*, 2018, **29**, 1807326.
13 X. Ling, W. J. Fang, Y.-H. Lee, P. T. Araujo, X. Zhang, J. F. Rodriguez-Nieva, Y. X. Lin, J. Zhang, J. Kong and M. S. Dresselhaus, *Nano Lett.*, 2014, **14**, 3033.
14 S. A. Ghopry, M. A. Alamri, R. Goul, R. Sakidja and J. Z. Wu, *Adv. Opt. Mater.*, 2019, **7**, 1801249.
15 S. Guo, Y. Zhang, Y. Ge, S. Zhang, H. Zeng and H. Zhang, *Adv. Mater.*, 2019, **31**, 1902352.
16 R. T. Lv, M. C. d. Santos, C. Antonelli, S. M. Feng, K. Fujisawa, A. Berkdemir, R. Cruz-Silva, A. L. Elias, N. Perea-Lopez, F. Lopez-Urias, H. Terrones and M. Terrones, *Adv. Mater.*, 2014, **26**, 7593.
17 Y. Yin, P. Miao, Y. M. Zhang, J. C. Han, X. H. Zhang, Y. Gong, L. Gu, C. Y. Xu, T. Yao, P. Xu, Y. Wang, B. Song and S. Jin, *Adv. Funct. Mater.*, 2017, **27**, 1606694.
18 Y. R. Liu, Z. B. Gao, M. Chen, Y. Tan and F. Chen, *Adv. Funct. Mater.*, 2018, **28**, 1805710.
19 E. Er, H.-L. Hou, A. Criado, J. Langer, M. Möller, N. Erk, L. M. Liz-Marzán and M. Prato, *Chem. Mater.*, 2019, **31**, 5725.
20 B. P. Majee, S. Mishra, R. K. Pandey, R. Prakash and A. K. Mishra, *J. Phys. Chem. C*, 2019, **123**, 18071.
21 M. Z. Li, X. C. Fan, Y. M. Gao and T. Qiu, *J. Phys. Chem. Lett.*, 2019, **10**, 4038.
22 X. Y. Hou, X. Y. Zhang, Q. W. Ma, X. Tang, Q. Hao, Y. C. Cheng and T. Qiu, *Adv. Funct. Mater.*, 2020, 1910171.
23 X. J. Song, Y. Wang, F. Zhao, Q. C. Li, H. Q. Ta, M. H. Rummeli, C. G. Tully, Z. Z. Li, W.-J. Yin, L. T. Yang, K.-B. Lee, J. Yang, I. Bozkurt, S. W. Liu, W. J. Zhang and M. Chhowalla, *ACS Nano*, 2019, **13**, 8312.
24 L. Tao, K. Chen, Z. F. Chen, C. X. Cong, C. Y. Qiu, J. J. Chen, X. M. Wang, H. J. Chen, T. Yu, W. G. Xie, S. Z. Deng and J.-B. Xu, *J. Am. Chem. Soc.*, 2018, **140**, 8696.
25 W. Tao, N. Kong, X. Ji, Y. Zhang, A. Sharma, J. Ouyang, B. Qi, J. Wang, N. Xie, C. Kang, H. Zhang, O. C. Farokhzad and J. S. Kim, *Chem. Soc. Rev.*, 2019, **48**, 2891.
26 Y. J. Gong, G. L. Ye, S. F. Lei, G. Shi, Y. M. He, J. H. Lin, X. Zhang, R. Vajtai, S. T. Pantelides, W. Zhou, B. Li and P. M. Ajayan, *Adv. Funct. Mater.*, 2016, **26**, 2009.
27 G. Kresse and J. Furthmüller, *Comput. Mater. Sci.*, 1996, **6**, 15.
28 X.-G. Xiong and T. Yanai, *J. Chem. Theory Comput.*, 2017, **13**, 3236.
29 L. Chaput, A. Togo and I. Tanaka, *Phys. Rev. B*, 2019, **100**, 174304.

30 J. P. Perdew, K. Burke and M. Ernzerhof, *Phys. Rev. Lett.*, 1996, **77**, 3865.
31 J. P. Perdew, M. Ernzerhof and K. Burke, *J. Chem. Phys.*, 1996, **105**, 9982.
32 S. Grimme, *J. Comput. Chem.*, 2006, **27**, 1787.
33 J. D. Zhou, J. H. Lin, X. W. Huang, Y. Zhou, Y. Chen, J. Xia, H. Wang, Y. Xie, H. M. Yu, J. C. Lei, D. Wu, F. C. Liu, Q. D. Fu, Q. S. Zeng, C.-H. Hsu, C. L. Yang, L. Lu, T. Yu, Z. X. Shen, H. Lin, B. I. Yakobson, Q. Liu, K. Suenaga, G. T. Liu and Z. Liu, *Nature*, 2018, **556**, 355.
34 S. S. Li, S. F. Wang, D.-M. Tang, W. J. Zhao, H. L. Xu, L. Q. Chu, Y. Bando, D. Golberg and G. Eda, *Appl. Mater. Today*, 2015, **1**, 60.
35 P. F. Yang, X. L. Zou, Z. P. Zhang, M. Hong, J. P. Shi, S. L. Chen, J. P. Shu, L. Y. Zhao, S. L. Jiang, X. B. Zhou, Y. H. Huan, C. Y. Xie, P. Gao, Q. Chen, Q. Zhang, Z. F. Liu and Y. F. Zhang, *Nat. Commun.*, 2018, **9**, 979.
36 J. Y. Jia, S. Jeon, J. Jeon, J. Xu, Y. J. Song, J. H. Cho, B. H. Lee, J. D. Song, H.-J. Kim, E. Hwang and S. Lee, *Small*, 2018, **14**, 1703065.
37 J. Jeon, J. Lee, G. Yoo, J. H. Park, G. Y. Yeom, Y. H. Jang and S. Lee, *Nanoscale*, 2016, **8**, 16995.
38 D. M. Seo, J.-H. Lee, S. Lee, J. Seo, C. Park, J. Nam, Y. Park, S. Jin, S. Srivastava, M. Kumar, Y. M. Jung, K.-H. Lee, Y.-J. Kim, S. Yoon, Y. L. Kim, P. M. Ajayan, B. K. Gupta and M. G. Hahm, *ACS Photonics*, 2019, **6**, 1379.
39 Q. G. Gao, Z. F. Zhang, X. L. Xu, J. Song, X. F. Li and Y. Q. Wu, *Nat. Commun.*, 2018, **9**, 4778.
40 H. Wang, X. W. Huang, J. H. Lin, J. Cui, Y. Chen, C. Zhu, F. C. Liu, Q. S. Zeng, J. D. Zhou, P. Yu, X. W. Wang, H. Y. He, S. H. Tsang, W. B. Gao, K. Suenaga, F. C. Ma, C. L. Yang, L. Lu, T. Yu, E. H. T. Teo, G. T. Liu and Z. Liu, *Nat. Commun.*, 2017, **8**, 394.
41 Z. Li, W. C. Yang, Y. Losovyj, J. Chen, E. Z. Xu, H. M. Liu, M. Werbianskyj, H. A. Fertig, X. C. Ye and S. X. Zhang, *Nano Res.*, 2018, **11**, 5978.
42 H. Liu, Y. Li, M. Xiang, H. Zeng and X. Shao, *ACS Nano*, 2019, **13**, 6083.
43 H. H. Lin, Q. Zhu, D. J. Shu, D. J. Lin, J. Xu, X. L. Huang, W. Shi, X. X. Xi, J. W. Wang and L. B. Gao, *Nat. Mater.*, 2019, **18**, 602.
44 T. Chen, G. Hao, G. Wang, B. Li, L. Kou, H. Yang, X. Zheng and J. Zhong, *2D Mater.*, 2019, **6**, 025002.
45 J. Seo, J. Lee, Y. Kim, D. Koo, G. Lee and H. Park, *Nano Lett.*, 2020, **20**, 1620.
46 S. M. Feng, M. C. d. Santos, B. R. Carvalho, R. T. Lv, Q. Li, K. Fujisawa, A. Laura Elia, Y. Lei, N. Perea-Lopez, M. Endo, M. H. Pan, M. A. Pimenta and M. Terrones, *Sci. Adv.*, 2016, **2**, 1600322.
47 J. Wang, Y. Yang, H. Li, J. Gao, P. He, L. Bian, F. Dong and Y. He, *Chem. Sci.*, 2019, **10**, 6330.
48 G. Li, W.-B. Gong, T. Qiu, S. Cong, Z. Zhao, R. Ma, Y. Michiue, S. Takayoshi and F. Geng, *ACS Appl. Nano Mater.*, 2020, **12**, 23523.
49 L. F. Sun, H. L. Hu, D. Zhan, J. X. Yan, L. Liu, J. S. Teguh, E. K. Yeow, P. S. Lee and Z. X. Shen, *Small*, 2014, **10**, 1090.
50 P. Miao, J.-K. Qin, Y. F. Shen, H. M. Su, J. F. Dai, B. Song, Y. C. Du, M. T. Sun, W. Zhang, H.-L. Wang, C.-Y. Xu and P. Xu, *Small*, 2018, **14**, 1704079.
51 X. Ling and J. Zhang, *Small*, 2010, **6**, 2020.
52 S. H. Zhao, T. Hotta, T. Koretsune, K. Watanabe, T. Taniguchi, K. Sugawara, T. Takahashi, H. Shinohara and R. Kitaura, *2D Mater.*, 2016, **3**, 025027.
53 S. S. Chee, W. J. Lee, Y. R. Jo, M. K. Cho, D. Chun, H. Baik, B. J. Kim, M. H. Yoon, K. Lee and M. H. Ham, *Adv. Funct.Mater.*, 2020, 1908147.
54 L. Nguyen, H.-P. Komsa, E. Khestanova, R. J. Kashtiban, J. J. Peters, S. Lawlor, A. M. Sanchez, J. Sloan, R. V. Gorbachev, I. V. Grigorieva, A. V. Krasheninnikov and S. J. Haigh, *ACS Nano*, 2017, **11**, 2894.
55 G. E. Myers and G. L. Montet, *J. Appl. Phys.*, 1970, **41**, 4642.
56 A. C. Walker and D. R. Tukket, *J. Phys. C: Solid State Phys.*, 1971, **4**, 378.
57 J. Yan, J. Xia, X. Wang, L. Liu, J. L. Kuo, B. K. Tay, S. Chen, W. Zhou, Z. Liu and Z. X. Shen, *Nano Lett.*, 2015, **15**, 8155.
58 T. Xue, W. Liang, Y. Li, Y. Sun, Y. Xiang, Y. Zhang, Z. Dai, Y. Duo, L. Wu, K. Qi, B. N. Shivananju, L. Zhang, X. Cui, H. Zhang and Q. Bao, *Nat. Commun.*, 2019, **10**, 28.
59 P. Wan, X. Wen, C. Sun, B. K. Chandran, H. Zhang, X. Sun and X. Chen, *Small*, 2015, **11**, 5409.